Materials Today Bio 32 (2025) 101682

Contents lists available at ScienceDirect

Materials Today Bio

journal homepage: www.journals.elsevier.com/materials-today-bio

Novel intravenous formulation for radiosensitization in osteosarcoma treatment

Haitao Zeng [a,b,1], Huixiong Feng [c,1], Chong Zhang [d,1], Zhe Kang [a], Jianping Wu [a], Xingqi Zhao [a], Anfei Huang [a], Yanyang Xu [f], Yufeng Huang [e,g,*], Hongwen Xu [a,**], Ming Gong [a,***]

[a] Department of Pediatric Orthopaedics, GuangZhou Women and Children's Medical Center, GuangZhou Medical University, Guangdong Provincial Clinical Research Center for Child Health, GuangZhou, 510623, China
[b] Bone&Soft Tissue Surgery, Hubei Cancer Hospital, Tongji Medical College, Huazhong University of Science and Technology, Wuhan, Hubei, 430079, China
[c] Department of Musculoskeletal Oncology, Sun Yat-sen University Cancer Center, Guangzhou 510060, China
[d] Department of Orthopedics, Renmin Hospital of Wuhan University, 430060 Wuhan, China
[e] Department of Cervical Spondylosis and Spine Orthopedics, The First Af Liated Hospital of Guangzhou University of Chinese Medicine, Guangzhou, China
[f] Department of Joint Surgery, Guangzhou First People's Hospital, School of Medicine, South China University of Technology, Guangzhou, 510180, China
[g] Guangdong Clinical Research Academy of Chinese Medicine, Guangzhou, China

ARTICLE INFO

Keywords:
Osteosarcoma
Radiosensitizer
Hafnium
Prussian blue
STING

ABSTRACT

Osteosarcoma (OS) is the most common primary malignant bone tumor in children and adolescents. While radiotherapy is an adjuvant treatment option for OS, particularly in cases of unresectable recurrent metastases, its efficacy remains limited. Enhancing radiosensitivity in OS cells is therefore crucial for improving treatment outcomes. Hafnium oxide, a known radiosensitizer, has demonstrated potential but its current formulation restricts its use to intratumoral administration, posing challenges for treating intraosseous tumors. The development of an intravenous formulation is thus highly desirable. Furthermore, radiotherapy resistance, driven by tumor hypoxia and an immunosuppressive microenvironment, further compromises its effectiveness. In this study, we synthesized hafnium-doped Prussian blue nanoparticles (HP) coated with a tannic acid-manganese metallophenol network (HPTM) to improve biocompatibility and enable intravenous administration. Following intravenous injection in a murine model of OS tibialis in situ tumors with lung metastases, HPTM effectively localized to the primary tumor. Within the acidic tumor microenvironment, manganese was released, activating the STING pathway and triggering anti-tumor immune responses. Moreover, near-infrared light irradiation of the Prussian blue component induced a photothermal effect, promoting apoptosis. Concurrently, under low-dose X-ray irradiation, HPTM augmented radiation energy deposition, generating reactive oxygen species and inducing DNA damage in tumor cells. This synergistic therapeutic approach significantly increased apoptosis in radiotherapy-resistant OS cells, reduced lung metastases, and suppressed primary tumor growth. These findings suggest a promising avenue for clinical translation, integrating radiosensitization, photothermal therapy, and STING pathway activation to overcome current limitations in OS radiotherapy.

1. Background

Osteosarcoma (OS) is the most common primary malignant bone tumor in children and adolescents, with a global incidence of 3.4 cases per million people annually [1,2]. Multidisciplinary approaches and multimodal chemotherapy have increased survival rates for patients undergoing surgical resection from 10-20 % to 60–70 %, a rate that has plateaued for over two decades [3,4]. Consequently, OS treatment has reached a bottleneck. For patients with recurrent metastases or those for whom surgical resection is challenging, available treatments include

* Corresponding author. Department of Cervical Spondylosis and Spine Orthopedics, The First Affliated Hospital of Guangzhou University of Chinese Medicine, Guangzhou, China.
** Corresponding author.
*** Corresponding author.
E-mail addresses: huangyf0602@163.com (Y. Huang), gzorthopedics@outlook.com (H. Xu), gomicom@163.com (M. Gong).
[1] These authors contribute equally to this work.

https://doi.org/10.1016/j.mtbio.2025.101682
Received 12 December 2024; Received in revised form 23 February 2025; Accepted 17 March 2025
Available online 18 March 2025

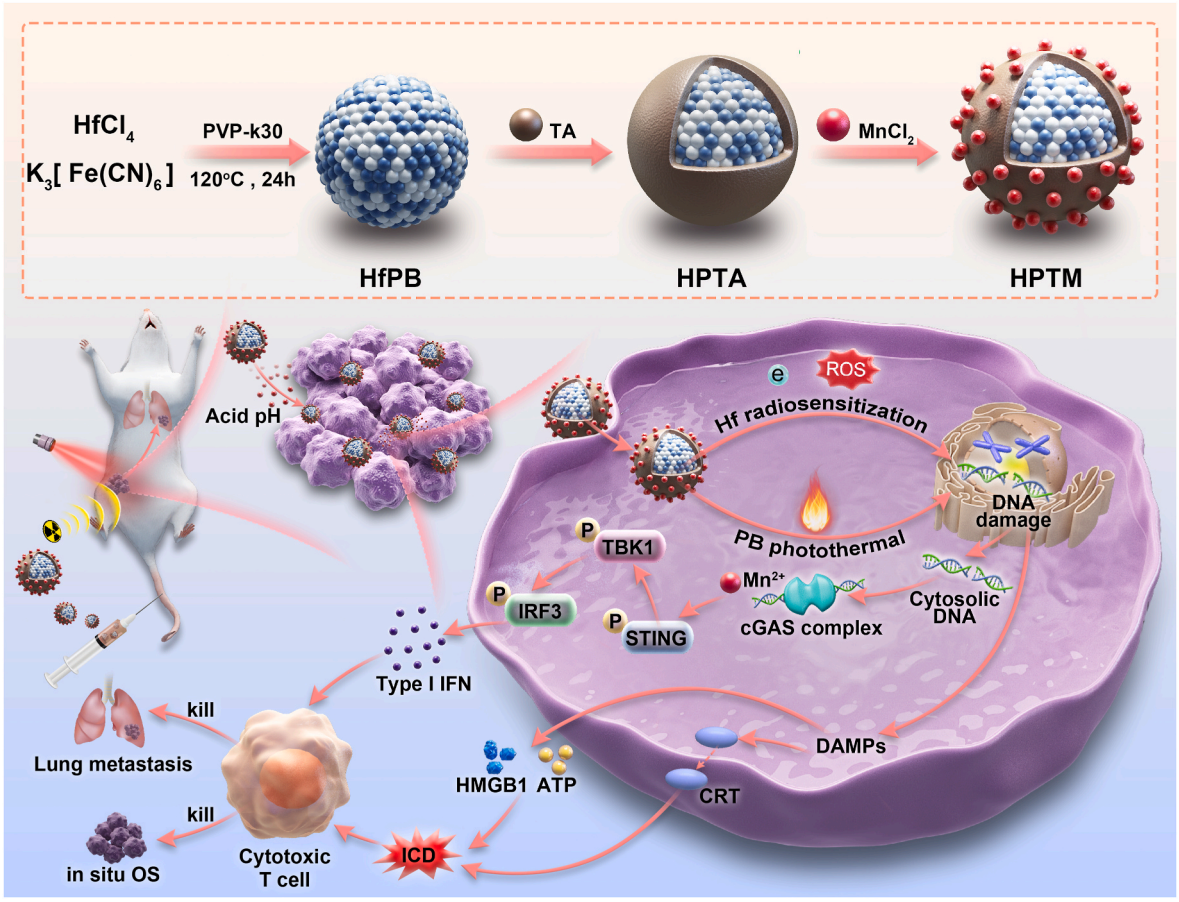

Scheme 1. Construction of hafnium-doped and manganese-loaded Prussian blue nanoparticles (HPTM) for cooperative cancer therapy of radiosensitization, photothermal therapy and STING activation.

chemotherapy, radiotherapy, and emerging targeted therapies and immunotherapy [5,6]. Radiotherapy is one of the most commonly employed techniques in oncology; for localized lesions, precision radiotherapy is often the preferred option [7,8]. Studies have shown a local control rate of 79.6 %, compared to 30 % in the general population [9]. Thus, enhancing the sensitivity of tumor cells to radiotherapy is a critical challenge that must be urgently addressed in tumor treatment (see Scheme 1).

Radiotherapy sensitization has emerged as a significant area of research within tumor nanomedicine in recent years [10,11]. High atomic number (high-z) elements can enhance the deposition of radiation energy within tumors, thereby improving sensitivity to radiotherapy [12,13]. This advancement has the potential to overcome the limitations associated with the current insensitivity of radiotherapy for OS. Hafnium oxide, recognized as a radiotherapy sensitizer, has progressed to clinical trial stages, promoting a higher rate of pathological complete response in locally advanced soft-tissue sarcoma [14–16]. These promising results encourage the use of hafnium oxide in radiotherapy for osteosarcoma. However, the current formulations of hafnium oxide in these trials are limited to intratumoral injections, posing challenges for targeting bone-located tumors and highlighting the urgent need for new dosage forms that can be administered intravenously.

Photothermal therapy (PTT) is an effective treatment modality for tumor suppression, as photothermal agents convert photons into heat that induces cell death in tumor cells at temperatures exceeding 42 °C [17,18]. Factors limiting the efficacy of tumor radiotherapy include local hypoxia within the tumor and damage to normal tissue cells from high-dose radiotherapy. The temperature-increasing properties of photothermal therapy can enhance tumor blood flow and alleviate hypoxia, thereby improving radiotherapy effectiveness. Consequently, photothermal therapy is regarded as a suitable method for augmenting radiotherapeutic effects [11,19]. Prussian blue (PB), an FDA-approved and biocompatible agent with favorable photothermal properties, is a promising adjuvant for hafnium-based radiosensitizers. It can ablate tumors, alleviate hypoxia, and enhance radiosensitivity [20–22].

The critical role of the cyclic GMP-AMP synthase (cGAS)-STING signaling pathway in tumors has been extensively investigated, revealing that its activation is essential for generating systemic antitumor immunity following radiotherapy [23,24]. Mn^{2+} activates the cGAS-STING pathway, thereby promoting dendritic cell maturation [25]. Tannic acid (TA) based metallophenolic network, a weakly acidic polyphenolic compound approved as a food additive by the U.S. FDA, possesses rich phenolic hydroxyl groups that confer a high density of negative charge in an aqueous medium [26]. This property facilitates strong interaction with metal cations, forming a metallophenolic network utilized in designing advanced functional materials for anti-tumor and antibacterial applications. The manganese-tannic acid network was employed to coat the outer layer of nanoparticles, enhancing biocompatibility, activating the STING pathway, improving MRI imaging, and augmenting the anti-tumor effects of nanoparticle-activated immunity [27–29].

This project proposes developing hafnium-doped Prussian blue nanoparticles (HfPB, HP) encapsulated with tannic acid (HPTA) and loaded with Mn^{2+} (HPTM) to form a metallophenolic network in the outer layer. Intravenously injected HPTM nanoparticles are designed to decompose within the acidic tumor microenvironment, releasing Mn^{2+}. This release is expected to stimulate the photothermal effect of PB and

enhance the radiosensitizing effect of Hf following irradiation with near-infrared light and X-rays. Additionally, this process aims to activate the STING pathway and induce immunogenic cell death (ICD), ultimately inhibiting the progression of osteosarcoma in situ and reducing lung metastasis (Scheme 1).

2. Materials and methods

2.1. Materials

Hafnium chloride, potassium ferricyanide, hydrochloric acid, normal melting point agarose, and low melting point agarose were purchased from Aladdin. DMEM with high glucose content, trypsin containing 0.25 % EDTA, and PBS buffer were obtained from Hyclone. Calcein-AM, propidium iodide, and an apoptosis kit were also procured.

2.2. Preparation of HPTM nanoparticles

Dissolve 264 mg of potassium ferricyanide and 3 g of polyvinylpyrrolidone (PVP) in 0.5 M hydrochloric acid (HCl). Next, add 264 mg of hafnium tetrachloride ($HfCl_4$) and stir the mixture thoroughly. Heat the mixture to 120 °C for 24 h, followed by an additional 24-h standing period. Centrifuge the mixture at 20,000 rpm for 15 min to obtain the precipitate. Wash the precipitate three times with both ethanol and water to isolate the hafnium-based Prussian blue (HfPB, HP) product(255 mg). Subsequently, redisperse the HfPB in water and add it dropwise to a 10 mg/mL aqueous tannic acid (TA) solution. Stir the mixture at 500 rpm for 30 min, then centrifuge at 12,000 rpm for 10 min to separate the hafnium-based Prussian blue-tannic acid (HPTA). Finally, dissolve the HPTA in water and add it dropwise to a 10 mg/mL aqueous manganese(II) chloride ($MnCl_2$) solution. Stir at 500 rpm for 30 min and centrifuge at 12,000 rpm for 10 min to isolate the hafnium-based Prussian blue-tannic acid-manganese (HPTM) product. Transmission electron microscopy (TEM) was utilized to examine the morphology and size of HPTM, while dynamic light scattering (DLS) was employed to measure the hydrodynamic diameter and zeta potential. Elemental mapping was conducted to analyze the distribution of Fe, Mn, and Hf. Additionally, X-ray photoelectron spectroscopy (XPS) was used to identify the absorption peaks of Fe, Mn, and Hf, and inductively coupled plasma optical emission spectrometry (ICP-OES) was applied to quantify the release of Mn and the loading content of Mn and Hf.

2.3. CCK8 assay

To assess the cytotoxicity of HPTM, cells including MC3T3, hFOB1.19, 293T, and RAW264.7 were seeded into 96-well plates at a density of 3500 cells per well and cultured for 24 h. Subsequently, increased concentrations of HPTM were added, and the incubation continued for an additional 24 h. The supernatant was then aspirated and discarded, and fresh culture medium containing 10 % CCK-8 (Meilunbio, China) was added, followed by incubation for 1 h at 37 °C. Absorbance was measured using an enzyme marker at 450 nm. The experimental groups for evaluating the anti-tumor effect included control, HPTM, HP + NIR + RT, RT, HPTM + NIR, HPTM + RT, and HPTM + NIR + RT. Radioresistant mouse OS cells (K7M2RR) were inoculated into 96-well plates and treated with 50 μg/mL of HP and HPTM, followed by incubation for 12 h prior to NIR irradiation (808 nm, 1 W/cm^2, 5 min) and radiotherapy irradiation (4 Gy). Absorbance at 450 nm was measured after 48–72 h using the same method.

2.4. Calcein-AM/PI staining

K7M2RR cells were inoculated into 24-well plates at a density of 4 × 10^4 cells per well and cultured for 24 h. Subsequently, HP and HPTM were added, and the cells were incubated for an additional 12 h. After 48–72 h, 2 μM calcein-AM and 50 μM propidium iodide (PI) staining solution were introduced, and the cells were incubated for 15 min in the dark. Images were then captured using a fluorescence microscope (Nikon, Japan).

2.5. Apoptosis

K7M2RR cells were inoculated into six-well plates at a density of 20 × 10^4 cells per well and cultured for 24 h. Following this, HP and HPTM were added, and the cells were incubated for an additional 12 h. NIR and X-ray irradiation were subsequently administered. After 48–72 h, dead cells in the supernatant were collected, and adherent cells were isolated through digestion with EDTA-free trypsin. The cells were then washed three times with ice - cold phosphate-buffered saline (PBS) and mixed with a 1 × loading buffer containing 5 μM fluorescein isothiocyanate (FITC) and 10 μM PI for an additional 30 min in the absence of light. The proportion of apoptotic cells was subsequently analyzed using flow cytometry (Beckman, USA).

2.6. Comet assay

To assess DNA damage in cells resulting from radiotherapy, we conducted comet assay. K7M2RR cells were inoculated into 24-well plates at a density of 4 × 10^4 cells per well and cultured for 24 h.Then 50 μg/mL HP and HPTM were added and incubated for an additional 12 h prior to near-infrared (NIR) irradiation (808 nm, 1 W/cm^2, 5min) and radiotherapy irradiation (4Gy). To prepare the agarose, we first created 100 μL of 0.7 % normal melting point agarose, boiled it, and applied it to a rough glass plate, ensuring a uniform coating with a coverslip, which was then cooled at 4 °C for 15 min. Next, we took 80 μL of 0.7 % low melting point agarose, mixed it with 20 μL of a cellular PBS suspension (with a cell density of 1.5 × 10^4), uniformly coated it with a coverslip, and allowed it to solidify at 4 °C for 15 min. After removing the coverslip, we added 100 μL of pre-warmed 0.7 % normal melting point agarose to form a second layer of gel, spreading it evenly before covering it with a coverslip and allowing it to solidify at 4 °C for 30 min. The coverslip was then removed, and the gel was washed three times with PBS. The gel was incubated with the lysis solution on ice for 1.5 h, followed by three washes with PBS. The gel was then placed in alkaline electrophoresis solution for 30 min and electrophoresed at 25 V for 20 min. Afterward, the gel was washed three times with PBS. Lastly, we soaked the gel slides in 1:10000 dilution of YeaRed nucleic acid dye (Yeasen, China), incubated for 15 min, covered with clean coverslips, and captured images under a fluorescence microscope.

2.7. Western blot

K7M2RR cells were seeded in six-well plates for 24 h. HP and HPTM were added, and the cells were incubated for an additional 12 h. Then 50 μg/mL HP and HPTM were added and incubated for an additional 12 h prior to NIR irradiation (808 nm, 1 W/cm^2, 5min) and the following radiotherapy irradiation (4Gy). Cells were lysed on ice using Radio-Immunoprecipitation Assay (RIPA) buffer for 15 min, followed by centrifugation at 14,000 rpm for 15 min to extract the proteins. The protein concentration was determined using a BCA kit. Enhanced chemiluminescence (ECL) imaging was performed following SDS-PAGE electrophoresis, membrane transfer, and incubation with primary and secondary antibodies. Antibody informations were as follows:Bcl-2 (AF6139), Bax (AF0120), γH2AX (AF3187), β-tubulin (AF7011), STING (DF12090), Phospho-STING (AF7416), TBK1(DF7026), Phospho-TBK1 (AF8190), IRF3 (DF6895), Phospho-IRF3 (AF2436) was purchased from Affinity Biosciences, USA.

2.8. In vitro photothermal imaging

Various concentrations of HPTM were injected in 1.5 mL centrifuge tubes and irradiated with 808 nm NIR light at a power density of 1 W/

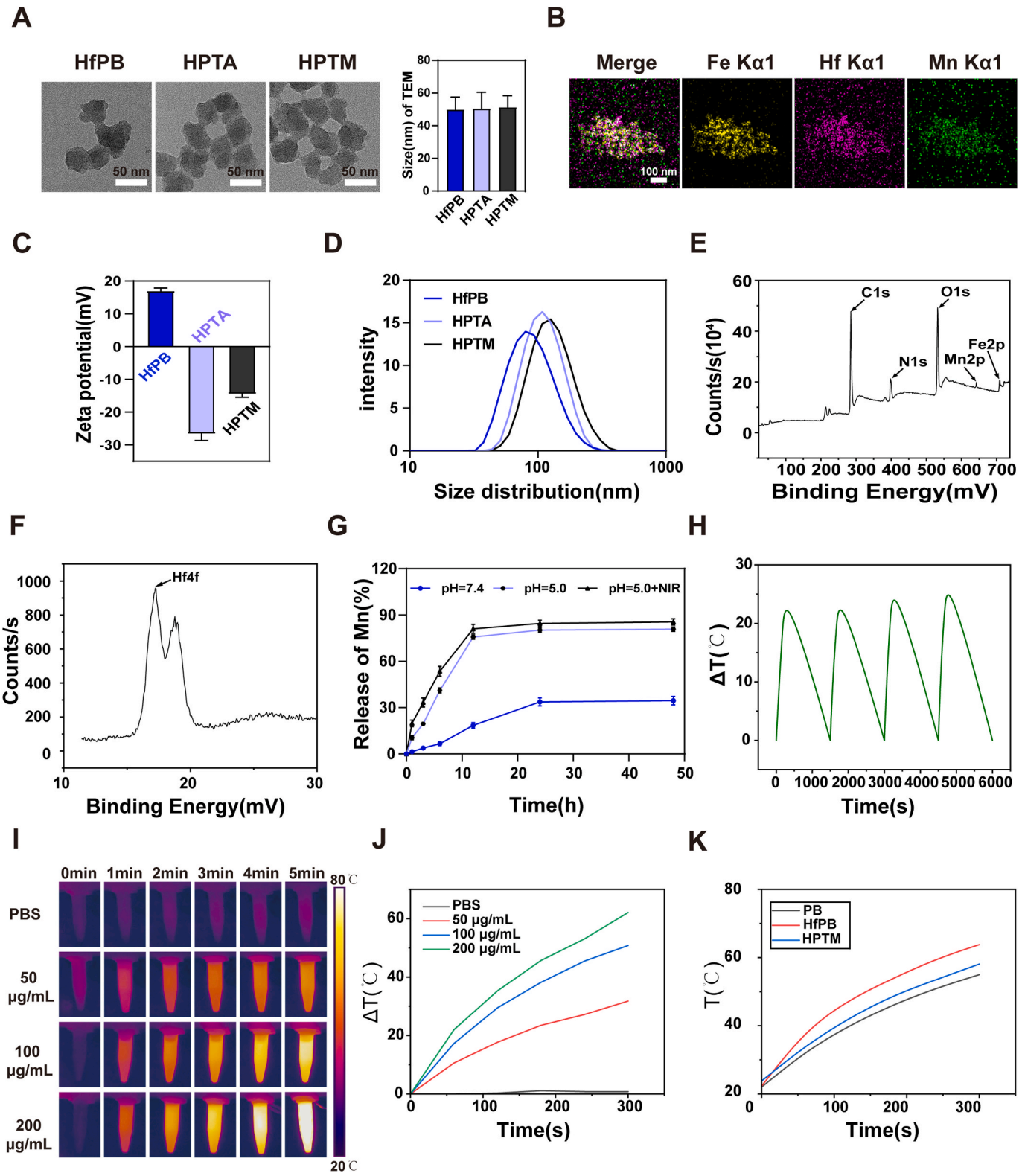

Fig. 1. Characterization of HPTM. (A) Transmission electron microscope (TEM) images and the size analysis of HfPB, HPTA and HPTM. (B) Elemental mapping images of HfPB, HPTA and HPTM. (C) The zeta potential (n = 3) and (D) size distribution of the HfPB, HPTA and HPTM PBM using Dynamic light scattering. (E–F) X-ray photoelectron spectra (XPS) for the HPTM. (G) The release curve of Mn using ICP-OES. (H) Temperature changes of HPTM for four laser on/off cycles. (I) Photothermal images and (J) heating curves of various concentrations of HPTM during laser irradiation at 808 nm for 5 min. (K) Heating curves of PB, HfPB, and HPTM (50 μg/mL) under 808 nm irradiation for 5 min.

cm^2 for 5 min. The resulting temperature changes were subsequently recorded using an infrared thermometer (Hikmicro, China).

2.9. Cellular uptake, fluorescence and flow cytometry

To investigate cellular uptake, HPTM was labeled with FITC. K7M2RR cells were seeded in 24-well plates and cultured for 24 h. Subsequently, HPTM-FITC was added and incubated for different durations. The cells were then fixed with 4 % paraformaldehyde and stained with a membrane dye-AF594 conjugated Wheat Germ Agglutinin (WGA, AAT Bioquest, USA). Following this, 5 μg/mL of 4′,6-diamidino-2-phenylindole (DAPI) staining solution (Beyotime, China) was applied to the cells for 5 min. Fluorescence images were acquired using a confocal microscope. For quantitative analysis of HPTM uptake, cells were seeded in six-well plates. After the addition of HPTM-FITC, the cells were digested and collected at different time points, and the percentage of FITC-positive cells was assessed by flow cytometry.

2.10. ICD marker detection

For calreticulin (CRT) immunofluorescence, K7M2RR cells were seeded onto a slide at a density of 4×10^4 cells per well and cultured for 24 h. Following this, 50 μg/mL HP and HPTM were added and the cells were incubated for an additional 12 h prior to NIR irradiation (808 nm, 1 W/cm^2, 5 min) and radiotherapy irradiation (4Gy). The cells were then fixed in 4 % paraformaldehyde, and a primary antibody against calreticulin (DF3139, Affinity Biosciences, USA), diluted at 1:200,was applied and incubated with the cells at 4 °C overnight. After washing with PBS, the cells were incubated with a YF®488 Goat Anti-Rabbit IgG (H&L) (UElandy, China) for 2 h. Finally, the nuclei were stained with DAPI. In parallel experiments, the culture supernatant of the cells was collected 48 h after irradiation with NIR and RT, and analyzed using an Enhanced ATP Assay Kit (Beyotime, China) and an HMGB1 ELISA kit (Solarbio, China).

2.11. Picogreen staining

Cells were seeded into 24-well plates and incubated overnight. Following the treatment protocol outlined earlier, the cells were washed three times with PBS. Picogreen (Yeasen, China) was diluted in PBS at a 1:200 ratio and incubated with the cells for 10 min. After incubation, the cells were washed again and stained with DAPI for 5 min. Finally, the cells were washed three times with PBS and imaged using a confocal microscope.

2.12. In vivo imaging

All the animal experiments were conducted according to the Laboratory animal-Guideline for ethical review of animal welfare approved by the Institutional Animal Care and Use Committee of Guangdong Medical Laboratory Animal center (NO. C202309-18). To evaluate whether HPTM can effectively target tumor lesions, we established a subcutaneous osteosarcoma model using 143B human osteosarcoma cells. The cells were cultured, digested, isolated, and then resuspended in PBS. Four-week-old Balb/c nude mice were selected, and 100 μL of cell suspension containing 2 million cells was injected subcutaneously into the left dorsal scapular region. After one week, mice with tumors measuring approximately 500 mm^3 were selected and randomly divided into two groups. These groups received tail vein injections of either IR780 or HPTM-IR780 (with an IR780 concentration of 2 mg/kg). Imaging was performed at various time points post-injection, followed by quantitative analysis of luminescence intensity.

2.13. In vivo anti-tumor effects

An in situ tumor model with lung metastasis was established using luciferase-labeled K7M2RR-Luc cells. The cells were cultured, digested with trypsin, resuspended in PBS, and injected into the right tibia of 3-week-old Balb/c mice at a concentration of 100,000 cells in 20 μL per mouse. Ten days later, tumor-bearing mice were identified using a live imaging system (PerkinElmer, USA) and randomly assigned to seven groups, each consisting of five mice: Control, HPTM, HP + NIR + RT, RT, HPTM + NIR, HPTM + RT, and HPTM + NIR + RT. HP (100 μL, 5 mg/kg) and HPTM (100 μL, 5 mg/kg) were administered and incubated for an additional 12 h prior to near-infrared (NIR) irradiation (808 nm, 1.5 W/cm^2, 5 min) and radiotherapy (6 Gy). Bioluminescence imaging was conducted at the beginning (Day 0) and end (Day 14) of the study by intraperitoneally injecting 100 μL of fluorescein potassium salt (Yeasen, China) into each mouse. Two weeks after treatment initiation, the mice were euthanized, and the tumors, along with critical organs, were excised, fixed in 4 % paraformaldehyde, sectioned, and stained with H&E. For immunofluorescence analysis, sections were incubated overnight with primary antibodies against CD8 (1:100, Affinity Biosciences, USA) and calreticulin (1:100, Affinity Biosciences, USA), followed by incubation with Alexa Fluor® 488-conjugated Goat Anti-Rabbit IgG (H + L) or Cy3-conjugated Goat Anti-Rabbit IgG (H + L) (1:100, Servicebio, China). TUNEL staining was performed using a TUNEL staining kit (Servicebio). For PCNA staining, sections were incubated overnight with PCNA antibody (1:100, Servicebio, China) and subsequently treated with Alexa Fluor® 488-conjugated Goat Anti-Rabbit IgG (H + L).

2.14. Statistical analysis

All data are presented as the mean ± standard deviation. Statistical analysis was conducted using one-way ANOVA with SPSS version 26.0. Differences were considered statistically significant when $p < 0.05$.

3. Results and discussion

3.1. Preparation and characterization of hafnium-doped and Mn^{2+}-loading Prussian blue nanoparticles (HPTM)

The scheme 1 outlines the synthetic construction and anti-tumor mechanism of hafnium-doped and manganese (Mn^{2+})-loaded Prussian blue nanoparticles (HPTM). Fig. 1 illustrates the morphological structure and physicochemical properties of HPTM. Transmission electron microscopy (TEM) images reveal an elliptical morphology and the size analysis for HP, HPTA, and HPTM (Fig. 1A). Uniform distributions of iron (Fe), hafnium (Hf), and manganese (Mn) were observed in the elemental mapping results (Fig. 1B). The zeta potentials of HP, HPTA, and HPTM were recorded at +17.08 mV, −26.74 mV, and −14.56 mV, respectively (Fig. 1C), indicating the successful encapsulation of tannic acid (TA) and the loading of manganese (Mn^{2+}). Dynamic light scattering (DLS) measurements showed an increased size distribution of HP, HPTA, and HPTM from 87.0 nm,103.0 nm–118.53 nm, respectively (Fig. 1D). According to XPS data, the HPTM displayed absorption peaks for Fe, Mn, and Hf (Fig. 1E and F). The loading contents of Hf and Mn were quantified by ICP-OES at 38.03 % and 10.38 %, respectively. An accelerated release of Mn was detected at pH 5.0 compared to pH 7.4, peaking at 12 h (Fig. 1G). Subsequent studies have demonstrated an increased release of manganese from HPTM following NIR irradiation. Conversely, RT showed minimal impact on Mn release (Fig. S1), indicating that elevated temperatures may facilitate the release of Mn. Fig. 1H shows that the photothermal effect of HPTM was not affected by periodic laser irradiation, with the observed temperature rise remaining nearly constant after four cycles of 808 nm NIR irradiation (1 W/cm^2, 5 min). The heating images and curves of HPTM depicted increasing temperatures corresponding to various concentrations post-irradiation, with a concentration of 50 μg/mL achieving a temperature rising of 31.7 °C (Fig. 1I and J). As the NIR power increases, the photothermal effect of HPTM is significantly enhanced (Fig. 1J and S2). In Fig. 1K, HfPB exhibits a higher photothermal temperature than Prussian blue,

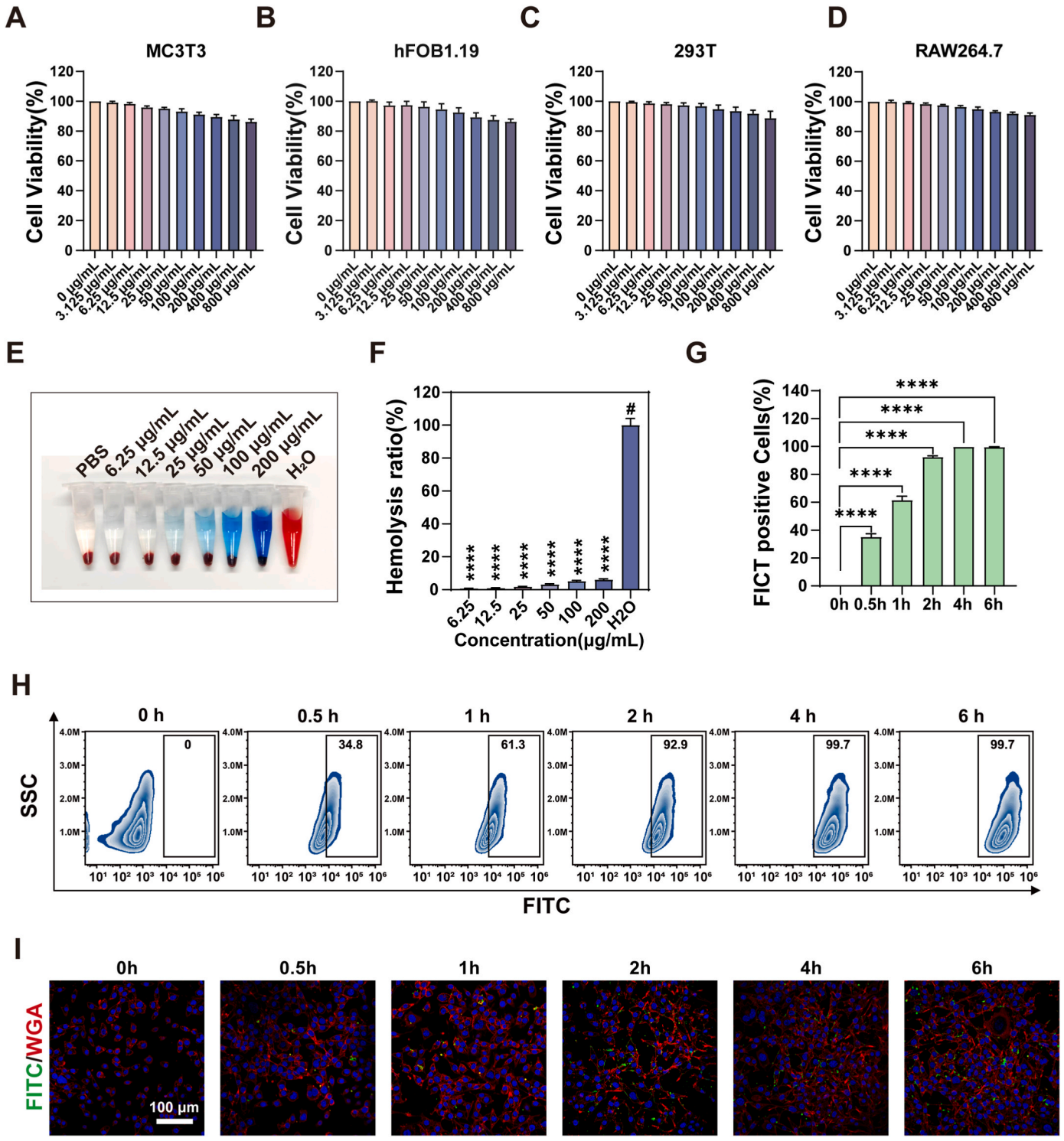

Fig. 2. Cytotoxicity and cell uptake of HPTM. (A–D) Cell viability of different non-tumor cells incubated with HPTM for 24h by CCK8 method. No significant differences were found between groups. (E–F) Images and quantitative analysis of in vitro hemolysis of red blood cells incubated with different concentration of HPTM. Deionized water and PBS acted as positive and negative control. (G–H) Tumor cells that uptake HPTM with IR780 was quantified by flow cytometry. (I) Observation of cellular uptake by a laser scanning confocal microscope (LSCM) at different time points. HPTM was modified with FITC (green). Cell membrane was stained with AF594-WGA (red). All experiments were carried out with 3 biological replicates. All values are the mean ± SD. P values, *p < 0.05, **p < 0.01, ***p < 0.001,****p < 0.0001. # indicates a group which was compared with other groups.

while HPTM exhibits an intermediate temperature. This phenomenon may account for the enhanced photothermal performance of HPTM observed after two cycles (Fig. 1H). The temperature increase likely promotes partial decomposition of the HPTM metal-phenol network, exposing more HfPB and thus enhancing the photothermal effect. The calculated photothermal conversion efficiency of HPTM (39.35 %) confirms its superior performance compared to Prussian blue and aligns with reported values for PB-based materials [30–32].

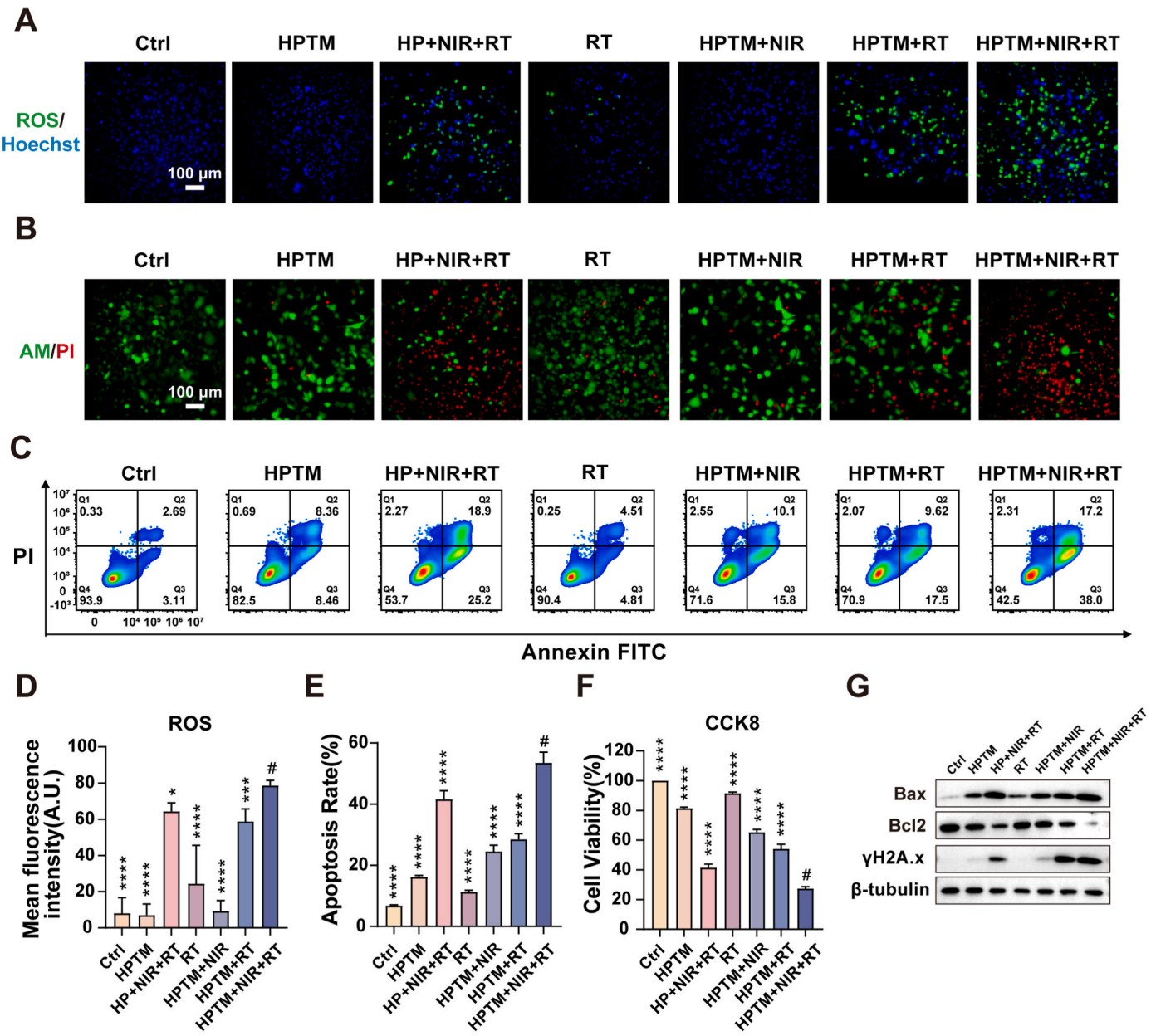

Fig. 3. Anti-OS effects of HPTM combined with NIR and RT. (A) Fluorescence microscopy images and (D) quantitative analysis of ROS in K7M2 cells which were stained with DCFH-DA after different treatments, including HPTM, HP + NIR + RT, RT, HPTM + NIR, HPTM + RT, HPTM + NIR + RT. (B) Live/dead cell staining was performed through Calcein AM (green)/PI (red) double staining method. (C, E) Evaluation of apoptosis rates of K7M2 cells treated with or without X-ray (4 Gy) in the presence or not the presence of NIR for 48h. (F) Cell viability was assessed by CCK8 method. (G) Expression of pro-apoptotic proteins Bax, anti-apoptotic proteins Bcl-2 and DNA double-strand breaks marker γH2A.x in K7M2RR OS cells after different treatment. All experiments were carried out with 3 biological replicates. # indicates a group which was compared with other groups. All values are the mean ± SD. P values, *p < 0.05, **p < 0.01, ***p < 0.001,****p < 0.0001.

3.2. Cytotoxicity and cellular uptake of HPTM

Prussian blue is an FDA-approved drug, and several studies have confirmed that doping with other elements such as copper, selenium, and gadolinium, allows Prussian blue to maintain low cytotoxicity and exhibit multifunctional ability [33–35]. And the doping of the metal ions may enhance the photothermal effect [36].Osteogenic precursor cells hFOB1.19, MC3T3, renal epithelial cells 293T, and RAW264.7 cells were selected to evaluate the cytotoxicity of HPTM and NIR. Data from the CCK8 assay indicated that even at a concentration of 800 μg/mL, HPTM did not significantly inhibit the viability of the various cell lines (Fig. 2A–D). Also, 5 min of NIR irradiation resulted in a slight reduction in cell viability (Fig. S3). Additionally, blood samples collected from 4-week-old Balb/c mice did not exhibit a color change in the supernatant after incubation with different concentrations of HPTM, and the extremely low hemolysis ratio suggests that intravenous injection of HPTM may be safe and feasible (Fig. 2E and F). Following the incubation of FITC-labeled HPTM with radioresistant osteosarcoma cells (K7M2RR), flow cytometry results revealed an increase in HPTM uptake by K7M2RR over time, peaking after 4 h (Fig. 2G and H). Confocal microscopy images demonstrated that the intracellular distribution of HPTM could be observed as early as 0.5 h post-uptake, peaking at 4 h (Fig. 2I).The results validate that HPTM exhibits superior biological safety and is capable of being efficiently internalized by osteosarcoma cells.

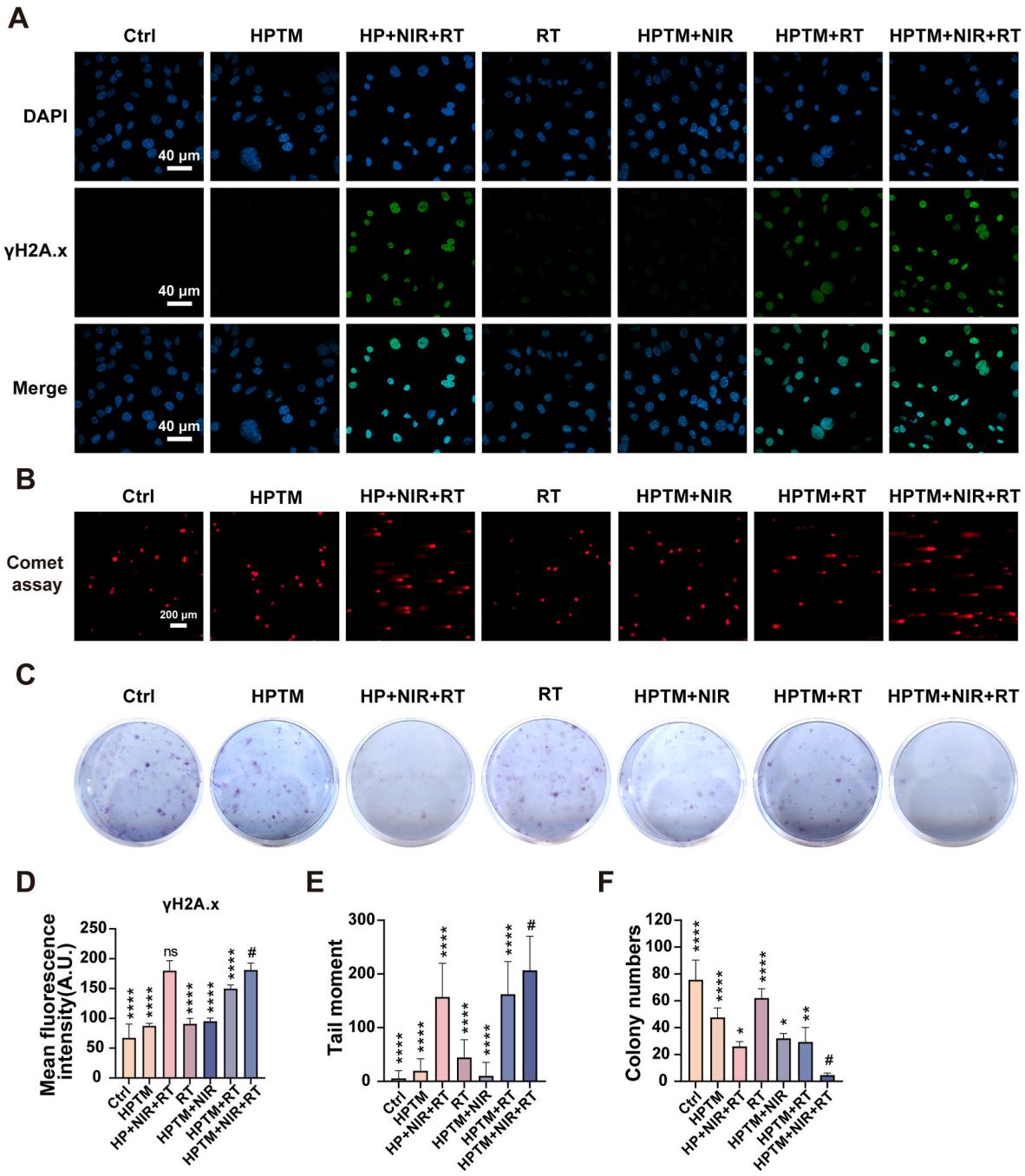

Fig. 4. In vitro studies of radioenhancer performance of HPTM. (A) Representative fluorescence images and (D) corresponding semi-quantitative analysis of intracellular γ-H2AX levels in K7M2 cells treated by different treatments, including HPTM, HP + NIR + RT, RT, HPTM + NIR, HPTM + RT, HPTM + NIR + RT. (B) Comet assays images and (E) tail movementafter K7M2 cells exposed to NIR and RT. (C) Colony formation assay images and (F) corresponding colony numbers of K7M2 cells after indicated treatments for ten days. All experiments were carried out with 3 biological replicates. # indicates a group which was compared with other groups. All values are the mean ± SD. P values, *$p < 0.05$, **$p < 0.01$, ***$p < 0.001$,****$p < 0.0001$. ns, not significant.

3.3. Anti-OS effects of HPTM combined with NIR and RT

During radiotherapy sensitization, X-rays interacting with hafnium release photoelectrons, Auger electrons, and Compton electrons, which are subsequently captured by water molecules localized in the tumor. This interaction generates hydroxyl radicals and induces DNA damage [37,38]. In this study, HPTM produced a substantial amount of reactive oxygen species (ROS) in cells following radiation stimulation, significantly exceeding the levels observed in the radiotherapy (RT) group. Additionally, near-infrared (NIR) light enhanced the production of ROS during radiotherapy, although NIR alone did not result in a significant increase in ROS (Fig. 3A–D). This observation suggests that the photothermal effect enhances the release of additional photons from the hafnium element, resulting in the production of increased reactive oxygen species, such as hydroxyl radicals, during radiotherapy. Furthermore, HPTM + NIR + RT exhibited greater ROS fluorescence compared to HP + NIR + RT. This likely stems from HP exacerbating mitochondrial damage under NIR and RT excitation, thereby enhancing Mn^{2+}-mediated reactive oxygen species generation via mitochondrial dysfunction [39]. AM/PI staining indicated that the combination of NIR and RT maximized the killing of tumor cells, surpassing the effectiveness of the HP + NIR + RT treatment. This suggests that the activation of the

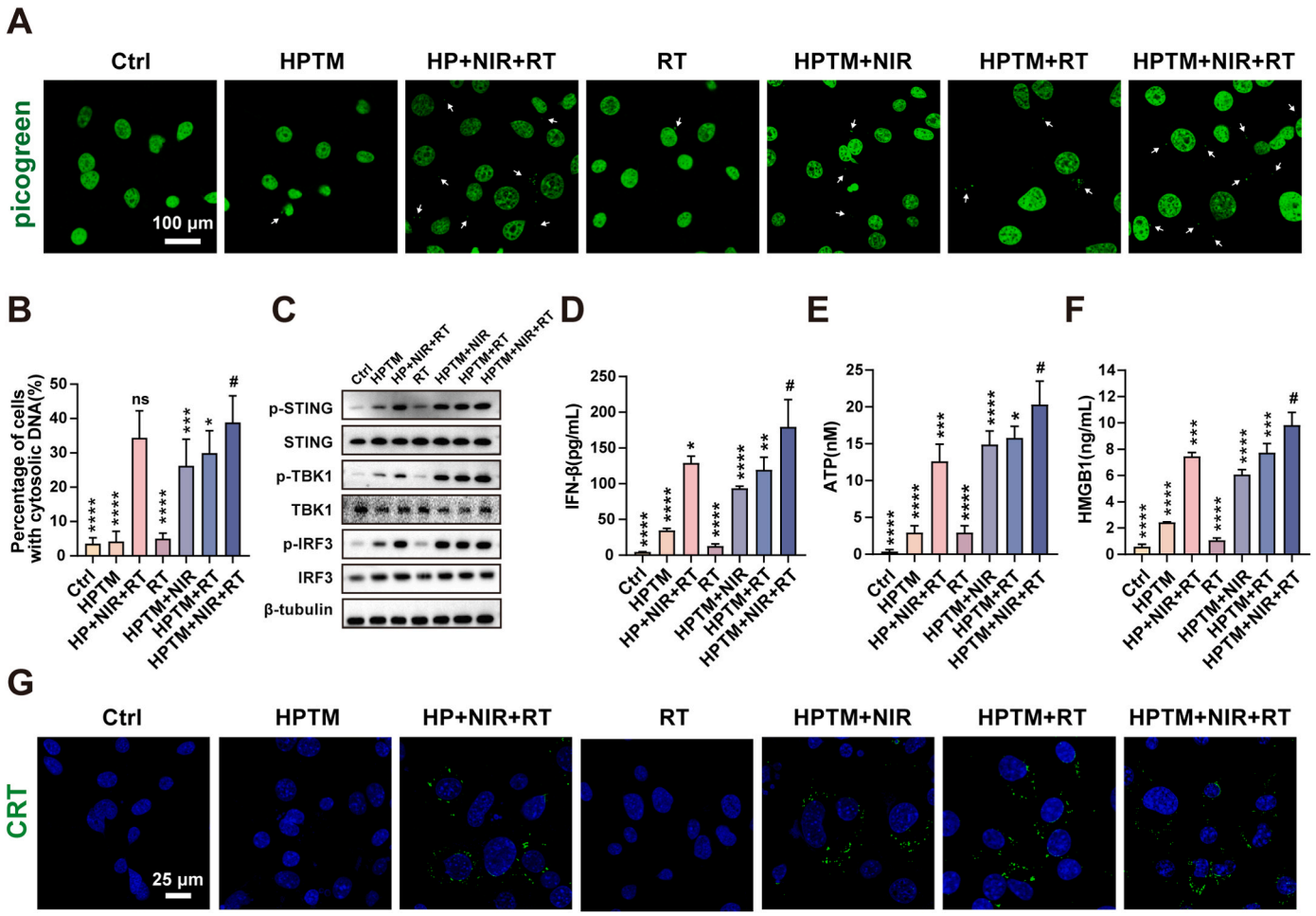

Fig. 5. HPTM with NIR and RT induced accumulation of cytosolic DNA, activation of cGAS-STING and ICD. (A) Representative fluorescence images and (B) quantitative analysis of Picogreen(green) staining of K7M2 cells treated by different treatments, including HPTM, HP + NIR + RT, RT, HPTM + NIR, HPTM + RT, HPTM + NIR + RT. (C) Activation of cGAS-STING related protein was measured by Western Blot. (D) Cytokine levels of IFN-γ in K7M2 cells by ELISA on day 3 post various treatments. (E) Released ATP and (F) HMGB1 were quantified through ATP detection kits and ELISA kits, respectively. (G) Calreticulin immunofluorescence on the outer surface of K7M2RR cells was imaged by LSCM. All experiments were carried out with 3 biological replicates. # indicates a group which was compared with other groups. All values are the mean ± SD, n = 3. P values, *p < 0.05, **p < 0.01, ***p < 0.001,****p < 0.0001. ns, not significant.

STING pathway by Mn^{2+} may promote the radiotherapy killing effect (Fig. 3B). Research on various tumors, including lung cancer, liver cancer, and sarcoma, indicates that the activation of the STING pathway, which targets DNA damage response, in conjunction with radiotherapy can promote the expression of additional cytokines, activate robust anti-tumor immunity, and ultimately enhance the efficacy of radiotherapy in eradicating tumor cells [40–42]. Flow cytometry revealed that the combination of HPTM, NIR, and RT induced the highest levels of apoptosis(Fig. 3C–E), a trend corroborated by CCK-8 results and Transwell migration assay(Fig. 3F and S4). It was also observed that the HPTM + NIR + RT treatment strongly stimulated the expression of the pro-apoptotic protein BAX while inhibiting the expression of the anti-apoptotic protein Bcl-2 (Fig. S5). The increased expression of γH2AX protein indicated that HPTM induced DNA damage with the assistance of NIR and RT(Fig. 3G and S5). These findings demonstrate that the combination of HPTM, NIR, and RT significantly enhances the antitumor effect.

3.4. *In vitro studies of radioenhancer performance of HPTM*

γ-H2AX is a widely recognized marker for detecting DNA double-strand break damage. Immunofluorescence analysis revealed stronger fluorescence in the HPTM + NIR + RT and HP + NIR + RT groups, indicating increased DNA damage. However, no statistically significant difference was observed between these two comparisons, suggesting that Mn^{2+} does not play a significant role in inducing DNA double-strand break damage. The fluorescence intensity in the HPTM + NIR + RT group was significantly higher than that in the HPTM + NIR group, demonstrating that the photothermal effect can more effectively stimulate the mechanisms of DNA damage induced by radiotherapy (Fig. 4A–D). In comet assay results, HPTM produced the most pronounced comet tail under the combined effects of NIR and RT, with statistical analysis indicating that this effect was significantly greater than that observed in the HP + NIR + RT group (Fig. 4B–E). These findings suggest that Mn^{2+} may enhance the radiotherapy damage of HPTM through mechanisms other than γ-H2AX related DNA double-strand breaks. The colony formation assay is a standard method for assessing the proliferative capacity of cells post-radiotherapy, evaluating their ability to undergo 'infinite' division and determining the long-term effects of ionizing radiation on their replicative potential [43, 44]. HPTM inhibited the proliferative ability of K7M2RR under both photothermal and radiotherapy conditions, although these effects were less pronounced than those observed in the combination group (Fig. 4C–F). These results underscore the strong radiosensitizing effect of HPTM following photothermal excitation.

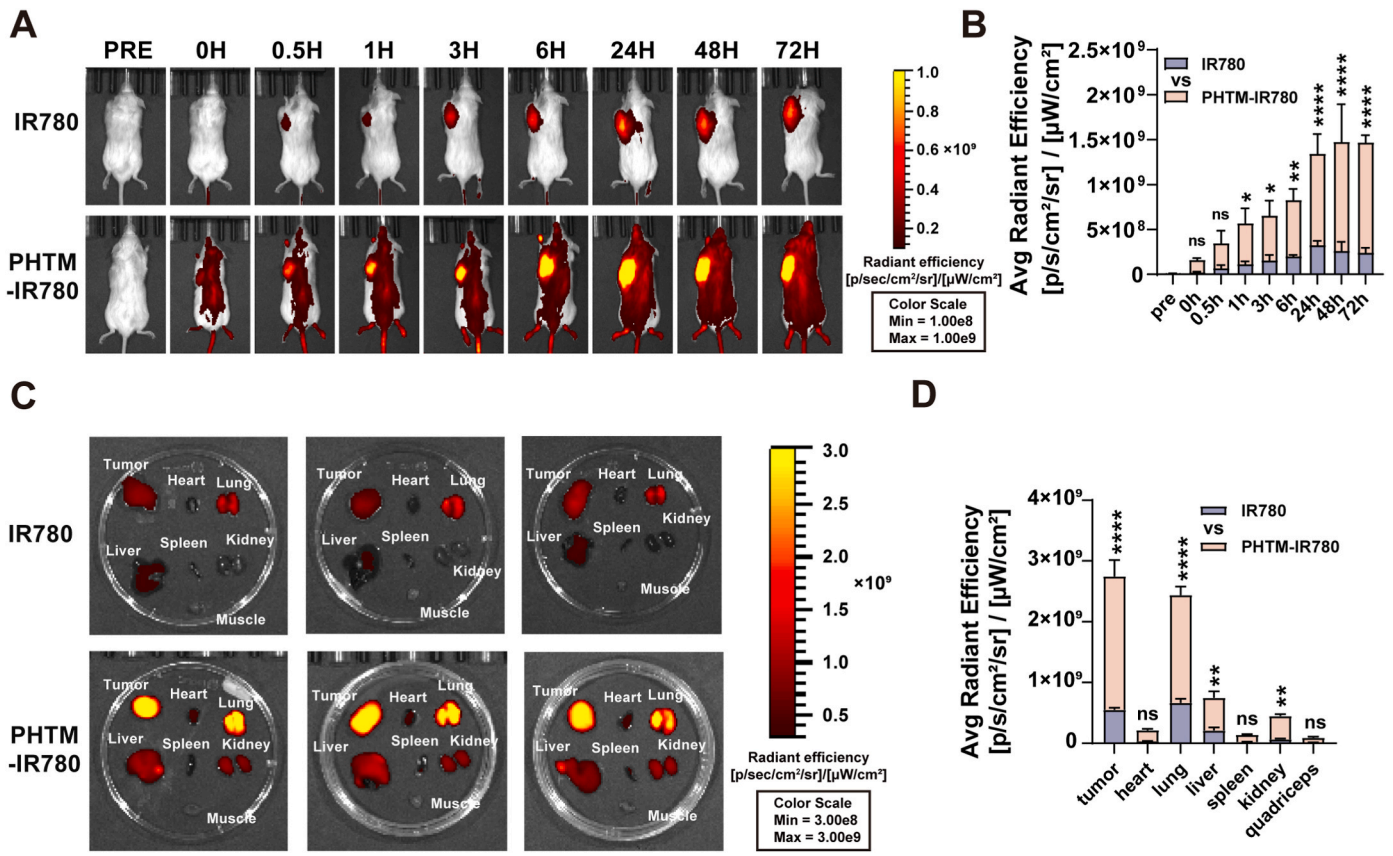

Fig. 6. In vivo distribution of HPTM in a subcutaneous OS tumor model. (A) In vivo and ex vivo fluorescence imaging of mice and (C) the major tissues after intravenous injection of IR780 and HPTM-IR780 for 0h,0.5h,1h, 3h, 6h, 24h, 48h and 72 h. (B) Quantitative analysis of fluorescence in mice and (D) organs. All values are the mean ± SD, n = 3. P values, *p < 0.05, **p < 0.01, ***p < 0.001,****p < 0.0001. ns, not significant.

3.5. HPTM with NIR and RT induced accumulation of cytosolic DNA, activation of cGAS-STING and ICD

Picogreen, a highly sensitive DNA staining reagent, is capable of detecting DNA within the cytoplasm [45,46]. The results of Picogreen staining presented in Fig. 5A and B indicate that both NIR radiation and RT alone can stimulate HPTM to promote the formation of cytoplasmic DNA; however, this effect is less pronounced than that observed with the combination of NIR and RT. Notably, HPTM alone did not demonstrate this effect. This implies that photothermal and radiotherapy effects cause damage to DNA, subsequently facilitating the formation of cytoplasmic DNA, whereas Mn^{2+} does not directly damage DNA. Additionally, Mn^{2+} plays a critical role in anti-tumor immunity by binding to cGAS, thereby increasing its sensitivity to double-stranded DNA (dsDNA) and enhancing its enzymatic activity.And, Mn^{2+} enhances the binding affinity of cGAMP to STING [47–49]. Furthermore, western blot analysis revealed that Mn^{2+} of HPTM could enhance the expression of pSTING, pTBK1, and pIRF3. Additionally, the HP + NIR + RT group also increased the expression of these proteins, possibly due to the increased formation of cytoplasmic DNA resulting from the combined effects of photothermal therapy and radiotherapy, which in turn activated the STING pathway. Ultimately, the combination of HPTM, NIR, and RT maximally promoted the activation of STING pathway proteins, underscoring the synergistic effects of NIR, RT, and Mn^{2+} in this process (Fig. 5C and S6). The activation of the STING pathway leads to the release of IFN-β, and the results presented in Fig. 5D suggest that the combination of Mn^{2+}, NIR, and RT optimally activated the STING pathway, with the medium supernatant releasing the highest levels of IFN-β. Regarding immunogenic cell death (ICD), ATP and HMGB1 levels in culture supernatants were assessed in this study. Neither RT nor HPTM alone could trigger potent release of ATP and HMGB1; however, HPTM significantly enhanced the secretion of these molecules following NIR and RT stimulation (Fig. 5E and F). Furthermore, immunofluorescence analysis of CRT in cells demonstrated that HPTM could induce more CRT translocation to the outside of the cell membrane with NIR or RT alone, or in combination, while no significant translocation occurred with HPTM alone (Fig. 5G). These findings suggest that Mn^{2+} does not directly activate CRT, and that the ICD-activating effect of HPTM is primarily dependent on the sensitizing effects of photothermal therapy and radiotherapy.

3.6. In vivo distribution of HPTM in a subcutaneous OS tumor model

The tumor - targeting efficacy of HPTM was examined using a subcutaneous OS tumor model. Following the intravenous injection of IR780-labeled HPTM into mice via the tail vein, the fluorescence intensity of the tumor gradually increased over time, peaking at 24 h, which was significantly higher than that observed in the IR780-only group (Fig. 6A and B). This finding indicates that HPTM can accumulate locally within the tumor. However, the data also revealed varying concentrations of HPTM in the lungs(Fig. 6C and D). The OS mouse models were derived from highly lung metastatic cells. Consequently, numerous micrometastases may have formed in the lung tissue, potentially accumulating HPTM and contributing to the observed high fluorescence signal in the lungs.

3.7. Anti-tumor effect of HPTM on in situ OS with pulmonary metastases model

The photothermal and antitumor effects of HPTM were evaluated in

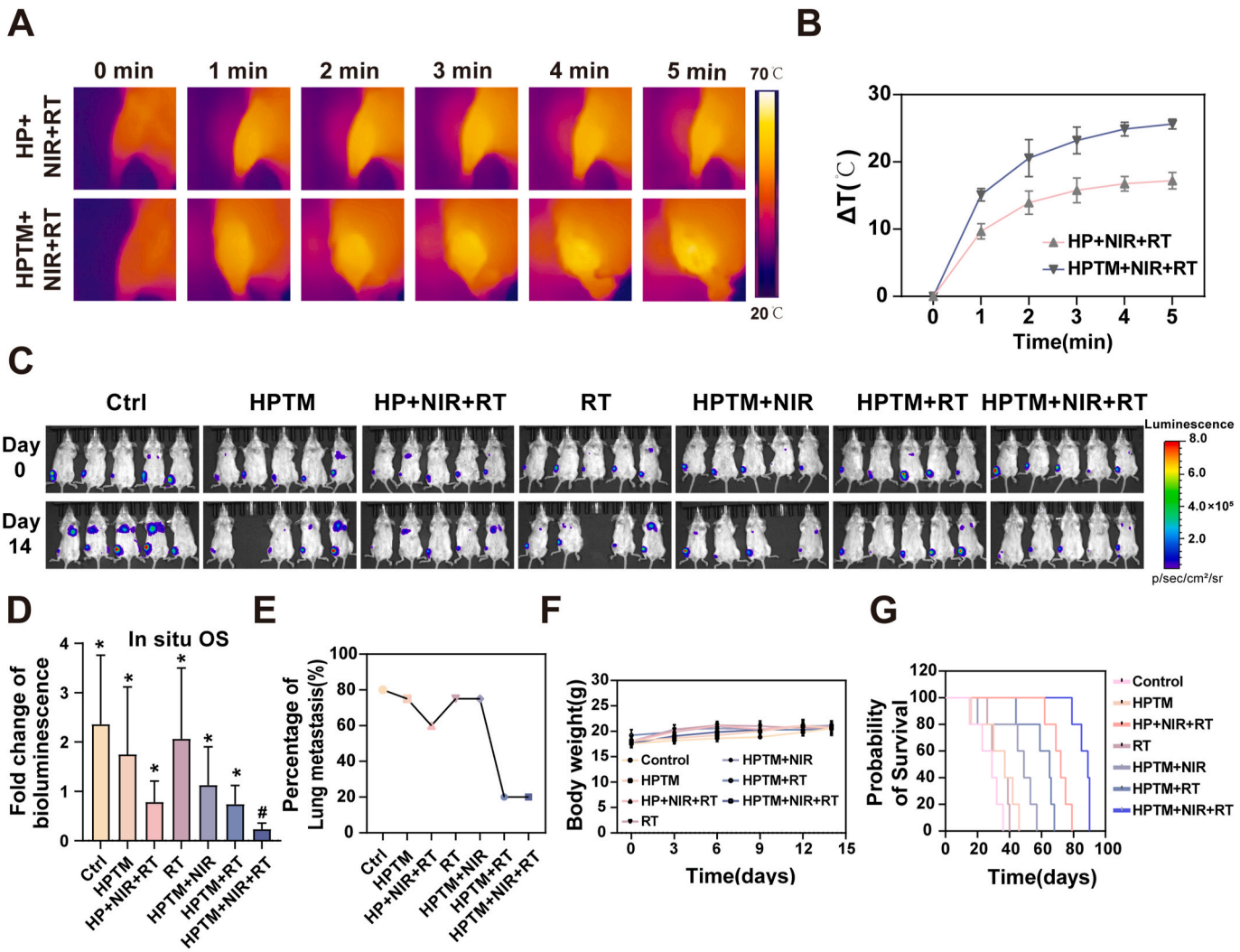

Fig. 7. Anti-tumor effect of HPTM on in situ OS with pulmonary metastases model. (A) NIR thermal images and (B) temperature profiles of in situ OS treated with HP + NIR + RT and HPTM + NIR + RT. (C) Representative bioluminescence images and (D) quantitative analysis of in situ OS and lung metastasis at 0 and 14 days after the first treatment. (E) Lung metastasis rate at day 14 by the bioluminescence method. (F) Bodyweight of the tumor-bearing mice with different treatments. (G) Lifespan of mice after indicated treatments in 90 d. (H) H&E and PCNA staining of in situ OS. Tindicates tumor tissue. B indicates bone. BM indicates bone marrow tissue. (I) H&E staining of lung metastasis, *$p < 0.05$, **$p < 0.01$. # indicates a group which was compared with other groups.

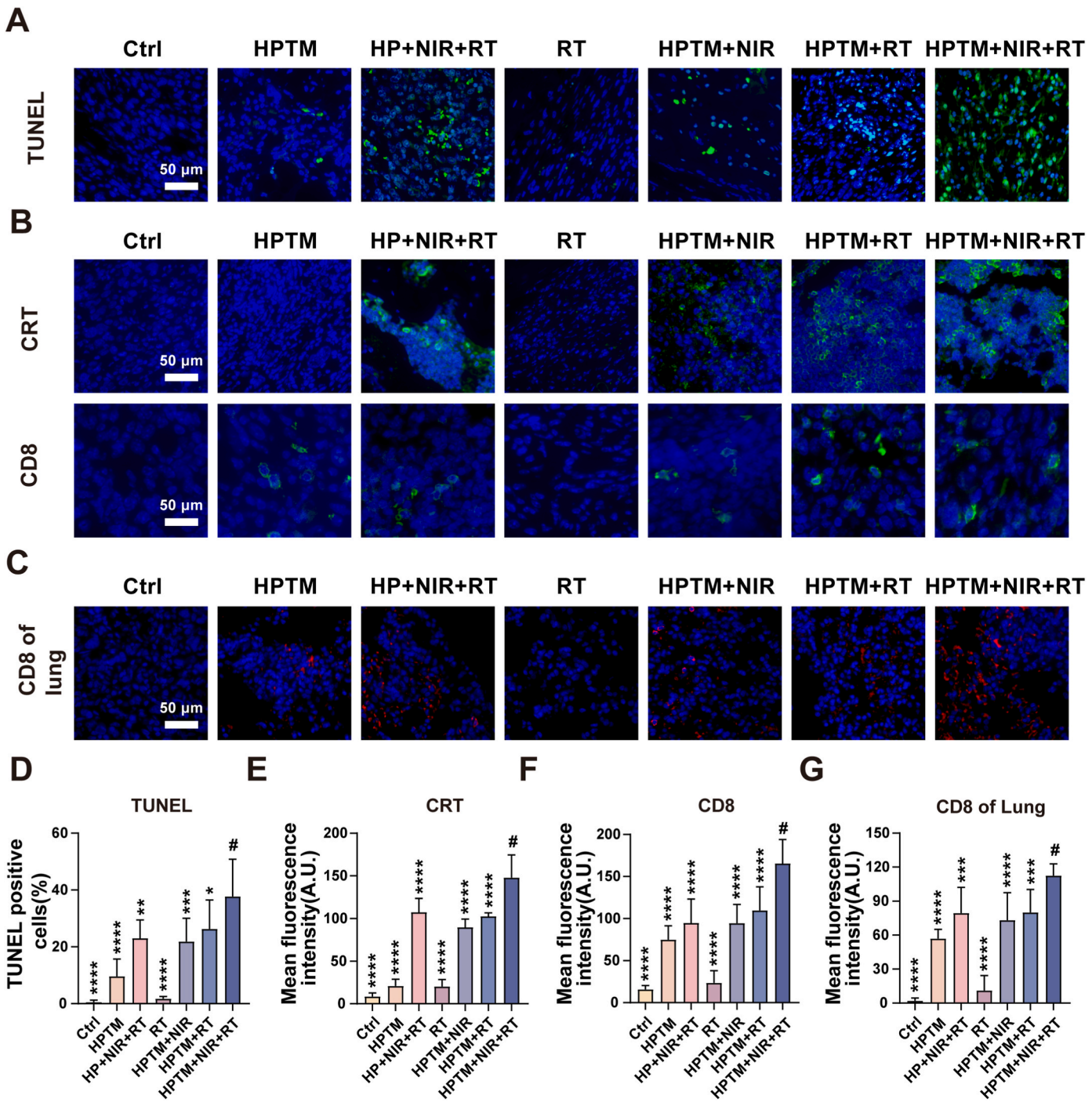

Fig. 8. (A) Representative images and (D) quantitative analysis of TUNEL staining for in situ OS. (B) Representative images and (E,F) quantitative analysis of CRT and CD8 staining for in situ OS. (C,G) Representative immunofluorescence images of CD8 for lung metastasis. All values are the mean ± SD,*P < 0.05. *p < 0.05, **p < 0.01, ***p < 0.001,****p < 0.0001. # indicates a group which was compared with other groups.

an in situ osteosarcoma model with lung metastasis. The NIR laser at 808 nm was set to a power of 1.5 W/cm^2, with an irradiation duration of 5 min. As illustrated in Fig. 7A and B, HPTM generated higher temperatures in osteosarcoma tissues due to its enhanced targeting ability, facilitated by tannic acid, compared to HP, resulting in a more effective photothermal response. Bioluminescence analysis of osteosarcoma cells indicated that mice in the HPTM + NIR + RT group exhibited the weakest luminescence of in situ tumors and the fewest lung metastases by day 14 (Fig. 7C and D). Although HPTM + NIR partially inhibited the growth of in situ tumors, lung metastases continued to progress. In contrast, the HPTM + RT group demonstrated fewer lung metastases, suggesting that radiotherapy may enhance anti-tumor immunity and mitigate the development of lung metastases. The inhibitory effects of HP + NIR + RT on in situ tumors were comparable to those of HPTM + NIR + RT; however, the impact on lung metastases was significantly reduced, indicating that the role of manganese in stimulating anti-tumor immunity requires the synergistic effects of NIR and RT (Fig. 7E). The osteosarcoma model, selected as an in situ tumor within the bone, presented challenges in directly observing differences in tumor size based on appearance (Fig. S7A). Simultaneously, no significant differences in the appearance of lung metastases could be observed (Fig. S7B). Therefore, we opted to use small animal *in vivo* imaging (Fig. 7C) and

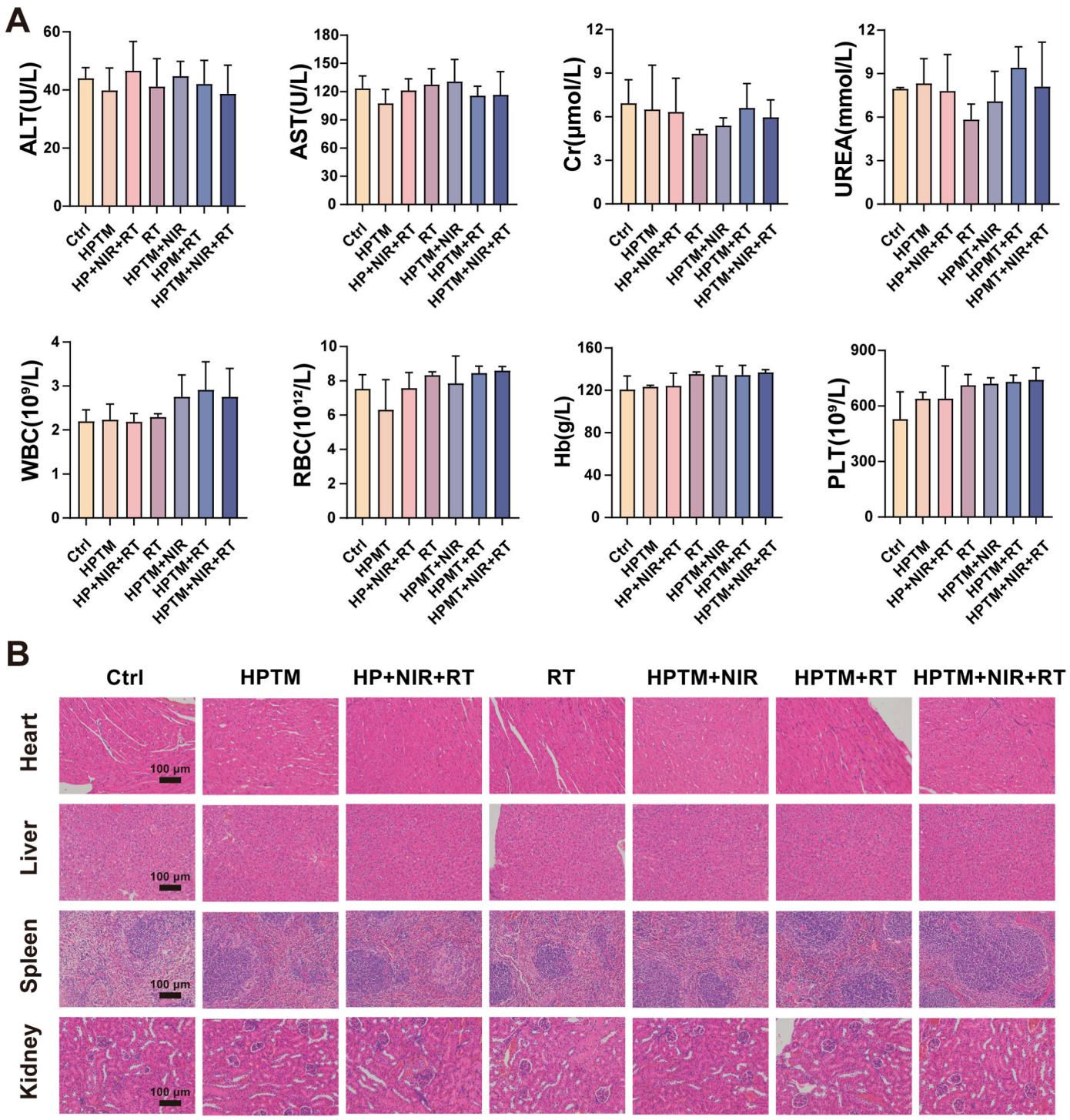

Fig. 9. (A) Serum biochemical index and blood routine index of various treatments in K7M2-bearing mice. There were no statistically significant differences between the groups. (B) Representative H&E images of major organs(heart, liver, spleen and kiney). Scale bars = 100 μm. All values are the mean ± SD.

H&E staining (Fig. 7I) to confirm the presence of lung metastases. Body weight data indicated slight effects of all treatments (Fig. 7F). Parallel experiments recorded the survival duration of the mice, revealing that those in the HPTM + NIR + RT group survived for nearly 90 days, thereby validating the efficacy of HPTM in anti-tumor treatment (Fig. 7G). H&E staining of in situ tumors in mice showed that the tumor area in the HPTM + NIR + RT group was the smallest among all groups (Fig. 7H). Immunohistochemical analysis of PCNA, a marker of cell proliferation, indicated that tumor cells in the RT and control groups exhibited high levels of PCNA expression. In contrast, only sporadic cells in the HPTM + NIR + RT group displayed PCNA expression, while a greater number of cells with high PCNA expression were observed in the HPTM + NIR group compared to the HPTM + RT group (Fig. 7H). These findings suggest that the photothermal effect alone has a limited capacity to inhibit tumor proliferation, and the superior radiosensitizing effect of HPTM may be attributed to the activation of anti-tumor immunity by radiotherapy. Consequently, HPTM demonstrated the most effective inhibition of tumor proliferation following NIR and RT treatment.

Additionally, TUNEL staining of in situ tumors indicated that HPTM

combined with NIR radiation and RT resulted in the largest area of apoptosis, surpassing that observed in the HPTM + NIR and HPTM + RT groups. In contrast, HPTM alone did not significantly induce apoptosis (Fig. 8A–D). Consistent with the immunofluorescence results observed in vitro, CRT staining corroborated that both the photothermal and radiosensitizing effects of HPTM effectively stimulated the translocation of CRT to the extracellular surface (Fig. 8B–E). An analysis of mouse blood HMGB1 yielded similar results to those observed in cellular experiments (Fig. S8). Furthermore, CD8 staining of in situ tumors demonstrated that HPTM combined with NIR and RT, as well as HPTM alone, facilitated the infiltration of cytotoxic CD8 T cells (Fig. 8B–F). This suggests that HPTM alone promotes CD8 T cell infiltration via the Mn-activated STING pathway, while the combination of HPTM with photothermal and radiosensitizing effects enhances CD8 T cell infiltration through the activation of both STING and ICD pathways.

Hematoxylin and eosin (H&E) staining of lung metastases indicated that HPTM and RT inhibited the development of lung metastases to a limited extent, resulting in slightly smaller metastases compared to the control group. Notably, significant lung metastases were challenging to identify in the lung tissues of the HPTM + NIR + RT group, whereas the lung metastases in the HPTM + RT group were smaller than those observed in the HPTM + NIR group (Fig. 7I). Further CD8 staining of lung tissues demonstrated that both the photothermal effect and radiotherapy sensitization could activate the body's anti-tumor immunity, promoting the infiltration of CD8 T cells into lung metastases, with the combination of both treatments proving to be more effective (Fig. 8C–G). Finally, we also isolated blood from the mice for safety analysis, which revealed no statistically significant differences across all indicators (Fig. 9A). Additionally, we isolated vital organs, including the lungs, hearts, livers, and kidneys, from each group of mice and performed H&E staining, which revealed no significant tissue necrosis and further confirmed the safety of HPTM (Fig. 9B).

HPTM synthesized in this study effectively inhibited osteosarcoma progression in vitro and in vivo, demonstrating the therapeutic potential of metals such as hafnium and manganese in oncology. Future studies will investigate HPTM's effects on various immune cell populations using single-cell sequencing and multicolor flow cytometry. While manganese is the most commonly reported metal activator of the STING pathway, exploring the role of other metals in STING activation could broaden the application of this pathway in cancer immunotherapy. A limitation of this study is the lack of in-depth investigation into the in vivo pharmacokinetics of HPTM. Future research will address this by characterizing the pharmacokinetic properties and circulatory stability of HPTM.

4. Conclusion

This study pioneers the investigation of hafnium-based radiosensitization for osteosarcoma treatment, incorporating advancements in hafnium formulation and delivery. We synthesized hafnium-doped Prussian blue nanoparticles loaded with Mn^{2+} (HPTM) exhibiting enhanced biocompatibility and cellular uptake. HPTM demonstrated potent radiosensitizing effects while retaining photothermal properties, inhibiting osteosarcoma cell proliferation and inducing apoptosis both in vitro and in vivo. Furthermore, HPTM stimulated intratumoral and intrapulmonary metastatic $CD8^+$ T cell responses. This immunostimulatory effect was mediated by Mn^{2+} activation of the STING pathway and ICD following combined photothermal and radiotherapy, ultimately augmenting tumor suppression in mice. These findings suggest that HPTM represents a promising alternative to conventional intratumoral injection of hafnium oxide and provides theoretical and experimental evidence for its potential application in the treatment of osteosarcoma and other intraosseous malignancies.

CRediT authorship contribution statement

Haitao Zeng: Writing – original draft, Investigation, Conceptualization. **Huixiong Feng:** Writing – original draft, Validation, Methodology. **Chong Zhang:** Validation, Methodology. **Zhe Kang:** Visualization. **Jianping Wu:** Supervision. **Xingqi Zhao:** Investigation. **Anfei Huang:** Validation. **Yanyang Xu:** Visualization. **Yufeng Huang:** Writing – review & editing, Conceptualization. **Hongwen Xu:** Writing – review & editing, Funding acquisition, Conceptualization. **Ming Gong:** Writing – review & editing, Funding acquisition, Conceptualization.

Declaration of competing interest

The authors declare that they have no known competing financial interests or personal relationships that could have appeared to influence the work reported in this paper.

Acknowledgements

The study was supported by the National Natural Science Foundation of China (Grant No. 82303806), GuangZhou Women and Children's Medical Center Research Program(Grant No. 2023BS016), Guangzhou Science and Technology Basic and Applied Basic Research Program (Grant No. 202201011108), Basic and Applied Basic Research Foundation of Guangdong Province (Grant No. 2023A1515220214), Natural Science Foundation of Hubei(Grant No. 2024AFB268).

Appendix A. Supplementary data

Supplementary data to this article can be found online at https://doi.org/10.1016/j.mtbio.2025.101682.

Data availability

Data will be made available on request.

References

[1] J. Ritter, S.S. Bielack, Osteosarcoma, Ann. Oncol. 21 (Suppl 7) (2010) vii320–325.
[2] S. Bielack, D. Carrle, P.G. Casali, et al., Osteosarcoma: ESMO clinical recommendations for diagnosis, treatment and follow-up, Ann. Oncol. 20 (Suppl 4) (2009) 137–139.
[3] N.M. Bernthal, N. Federman, F.R. Eilber, et al., Long-term results (>25 years) of a randomized, prospective clinical trial evaluating chemotherapy in patients with high-grade, operable osteosarcoma, Cancer 118 (2012) 5888–5893.
[4] S. Smeland, S.S. Bielack, J. Whelan, et al., Survival and prognosis with osteosarcoma: outcomes in more than 2000 patients in the EURAMOS-1 (European and American Osteosarcoma Study) cohort, Eur. J. Cancer 109 (2019) 36–50.
[5] P.S. Meltzer, L.J. Helman, New horizons in the treatment of osteosarcoma, N. Engl. J. Med. 385 (2021) 2066–2076.
[6] M.S. Isakoff, S.S. Bielack, P. Meltzer, et al., Osteosarcoma: current treatment and a collaborative pathway to success, J. Clin. Oncol. 33 (2015) 3029–3035.
[7] J.S. Tobias, Clinical practice of radiotherapy, Lancet 339 (1992) 159–163.
[8] Y. Wu, M. Yi, M. Niu, et al., Beyond success: unveiling the hidden potential of radiotherapy and immunotherapy in solid tumors, Cancer Commun. 44 (2024) 739–760.
[9] M.J. Spalek, J. Poleszczuk, A.M. Czarnecka, et al., Radiotherapy in the management of pediatric and adult osteosarcomas: a multi-institutional cohort analysis, Cells 10 (2021).
[10] H. Wang, X. Mu, H. He, et al., Cancer radiosensitizers, Trends Pharmacol. Sci. 39 (2018) 24–48.
[11] J. Liu, J. Wu, T. Chen, et al., Enhancing X-ray sensitization with multifunctional nanoparticles, Small 20 (2024) e2400954.
[12] L.R.H. Gerken, M.E. Gerdes, M. Pruschy, et al., Prospects of nanoparticle-based radioenhancement for radiotherapy, Mater. Horiz. 10 (2023) 4059–4082.
[13] Y. Liu, P. Zhang, F. Li, et al., Metal-based NanoEnhancers for future radiotherapy: radiosensitizing and synergistic effects on tumor cells, Theranostics 8 (2018) 1824–1849.
[14] S. Bonvalot, P.L. Rutkowski, J. Thariat, et al., NBTXR3, a first-in-class radioenhancer hafnium oxide nanoparticle, plus radiotherapy versus radiotherapy alone in patients with locally advanced soft-tissue sarcoma (Act.In.Sarc): a multicentre, phase 2-3, randomised, controlled trial, Lancet Oncol. 20 (2019) 1148–1159.

[15] C. Hoffmann, V. Calugaru, E. Borcoman, et al., Phase I dose-escalation study of NBTXR3 activated by intensity-modulated radiation therapy in elderly patients with locally advanced squamous cell carcinoma of the oral cavity or oropharynx, Eur. J. Cancer 146 (2021) 135–144.
[16] S. Bonvalot, C. Le Pechoux, T. De Baere, et al., First-in-Human study testing a new radioenhancer using nanoparticles (NBTXR3) activated by radiation therapy in patients with locally advanced soft tissue sarcomas, Clin. Cancer Res. 23 (2017) 908–917.
[17] J. Li, W. Li, L. Xie, et al., A metal-polyphenolic nanosystem with NIR-II fluorescence-guided combined photothermal therapy and radiotherapy, Chem. Commun. 57 (2021) 11473–11476.
[18] C. Feng, W. Zheng, Y. Jiang, et al., Au nanorods activated the Zn/Ce composites with cancer cell specific cytotoxicity for enhanced chemodynamic therapy, Nano Lett. 24 (2024) 295–304.
[19] H.E. Barker, J.T. Paget, A.A. Khan, et al., The tumour microenvironment after radiotherapy: mechanisms of resistance and recurrence, Nat. Rev. Cancer 15 (2015) 409–425.
[20] Y. Wang, Z. Liang, Z. Liang, et al., Advancements of Prussian blue-based nanoplatforms in biomedical fields: progress and perspectives, J. Contr. Release 351 (2022) 752–778.
[21] Z. Qin, Y. Li, N. Gu, Progress in applications of prussian blue nanoparticles in biomedicine, Adv. Healthcare Mater. 7 (2018) e1800347.
[22] Y. Yang, Q. Liu, M. Wang, et al., Genetically programmable cell membrane-camouflaged nanoparticles for targeted combination therapy of colorectal cancer, Signal Transduct. Targeted Ther. 9 (2024) 158.
[23] V.M. Kho, V.E. Mekers, P.N. Span, et al., Radiotherapy and cGAS/STING signaling: impact on MDSCs in the tumor microenvironment, Cell. Immunol. 362 (2021) 104298.
[24] M. McLaughlin, E.C. Patin, M. Pedersen, et al., Inflammatory microenvironment remodelling by tumour cells after radiotherapy, Nat. Rev. Cancer 20 (2020) 203–217.
[25] Z. Deng, M. Xi, C. Zhang, et al., Biomineralized MnO(2) nanoplatforms mediated delivery of immune checkpoint inhibitors with STING pathway activation to potentiate cancer radio-immunotherapy, ACS Nano 17 (2023) 4495–4506.
[26] Z. Guo, W. Xie, J. Lu, et al., Tannic acid-based metal phenolic networks for bio-applications: a review, J. Mater. Chem. B 9 (2021) 4098–4110.
[27] Y. Meng, J. Huang, J. Ding, et al., Mn-phenolic networks as synergistic carrier for STING agonists in tumor immunotherapy, Mater Today Bio 26 (2024) 101018.
[28] T. Liu, M. Zhang, W. Liu, et al., Metal ion/tannic acid assembly as a versatile photothermal platform in engineering multimodal nanotheranostics for advanced applications, ACS Nano 12 (2018) 3917–3927.
[29] J.H. Han, H.E. Shin, J. Lee, et al., Combination of metal-phenolic network-based immunoactive nanoparticles and bipolar irreversible electroporation for effective cancer immunotherapy, Small 18 (2022) e2200316.
[30] Y. Tian, Y. Li, J. Liu, et al., Photothermal therapy with regulated Nrf2/NF-kappaB signaling pathway for treating bacteria-induced periodontitis, Bioact. Mater. 9 (2022) 428–445.
[31] L. Cheng, H. Gong, W. Zhu, et al., PEGylated Prussian blue nanocubes as a theranostic agent for simultaneous cancer imaging and photothermal therapy, Biomaterials 35 (2014) 9844–9852.
[32] X. Xie, W. Gao, J. Hao, et al., Self-synergistic effect of Prussian blue nanoparticles for cancer therapy: driving photothermal therapy and reducing hyperthermia-induced side effects, J. Nanobiotechnol. 19 (2021) 126.
[33] W. Wu, L. Yu, Y. Pu, et al., Copper-enriched prussian blue nanomedicine for in situ disulfiram toxification and photothermal antitumor amplification, Adv. Mater. 32 (2020) e2000542.
[34] R. Qiao, Z. Yuan, M. Yang, et al., Selenium-doped nanoheterojunctions for highly efficient cancer radiosensitization, Adv. Sci. 11 (2024) e2402039.
[35] C. Zhang, Z. Xu, H. Di, et al., Gadolinium-doped Au@prussian blue nanoparticles as MR/SERS bimodal agents for dendritic cell activating and tracking, Theranostics 10 (2020) 6061–6071.
[36] H. Sun, R. Chang, Q. Zou, et al., Supramolecular protein nanodrugs with coordination- and heating-enhanced photothermal effects for antitumor therapy, Small 15 (2019) e1905326.
[37] M.R. Gill, K.A. Vallis, Transition metal compounds as cancer radiosensitizers, Chem. Soc. Rev. 48 (2019) 540–557.
[38] B. Chen, L. Xiao, W. Wang, et al., Bi(2-x)Mn(x)O(3) nanospheres engaged radiotherapy with amplifying DNA damage, ACS Appl. Mater. Interfaces 15 (2023) 33903–33915.
[39] E. Bonke, I. Siebels, K. Zwicker, et al., Manganese ions enhance mitochondrial H(2)O(2) emission from Krebs cycle oxidoreductases by inducing permeability transition, Free Radic. Biol. Med. 99 (2016) 43–53.
[40] Y. Long, J. Guo, J. Chen, et al., GPR162 activates STING dependent DNA damage pathway as a novel tumor suppressor and radiation sensitizer, Signal Transduct. Targeted Ther. 8 (2023) 48.
[41] W. Hong, Y. Zhang, S. Wang, et al., RECQL4 inhibits radiation-induced tumor immune awakening via suppressing the cGAS-STING pathway in hepatocellular carcinoma, Adv. Sci. 11 (2024) e2308009.
[42] W. Floyd, M. Pierpoint, C. Su, et al., Atrx deletion impairs CGAS/STING signaling and increases sarcoma response to radiation and oncolytic herpesvirus, J. Clin. Investig. 133 (2023).
[43] Q. Yang, B. Xie, H. Tang, et al., Minichromosome maintenance 3 promotes hepatocellular carcinoma radioresistance by activating the NF-kappaB pathway, J. Exp. Clin. Cancer Res. 38 (2019) 263.
[44] Z. Li, H. Xue, J. Li, et al., CDKL1 potentiates the antitumor efficacy of radioimmunotherapy by binding to transcription factor YBX1 and blocking PD-L1 expression in lung cancer, J. Exp. Clin. Cancer Res. 43 (2024) 89.
[45] C.D. Georgiou, I. Papapostolou, K. Grintzalis, Protocol for the quantitative assessment of DNA concentration and damage (fragmentation and nicks), Nat. Protoc. 4 (2009) 125–131.
[46] J. Xia, L. Wang, T. Shen, et al., Integrated manganese (III)-doped nanosystem for optimizing photothermal ablation: amplifying hyperthermia-induced STING pathway and enhancing antitumor immunity, Acta Biomater. 155 (2023) 601–617.
[47] M. Lv, M. Chen, R. Zhang, et al., Manganese is critical for antitumor immune responses via cGAS-STING and improves the efficacy of clinical immunotherapy, Cell Res. 30 (2020) 966–979.
[48] X. Sun, Y. Zhang, J. Li, et al., Amplifying STING activation by cyclic dinucleotide-manganese particles for local and systemic cancer metalloimmunotherapy, Nat. Nanotechnol. 16 (2021) 1260–1270.
[49] X. He, G. Gong, M. Chen, et al., Metal-phenolic nanocloaks on cancer cells potentiate STING pathway activation for synergistic cancer immunotherapy, Angew Chem. Int. Ed. Engl. 63 (2024) e202314501.